3D micro printed capillary electrospray thruster with a fully modular integrated extraction electrode

Fynn L. Kunze[1*] , Torsten Henning[1] and Peter J. Klar[1]

*Correspondence:
Fynn.Kunze@physik.uni-giessen.de

[1] Institute of Experimental
Physics I and Center
for Materials Research ZfM/
LaMa, Justus Liebig University,
Heinrich-Buff-Ring 16,
DE-35392 Giessen, Germany

Abstract

An internally wetted capillary-type electrospray thruster design is presented. The capillary emitters are optimized for fabrication using 3D micro lithography and can achieve sub 10-micrometer capillary diameters with an aspect ratio of over 20. Also provided is a design for a completely modular integrated extraction electrode that comprises an electrode carrier produced by 3D micro lithography and a thin metal film. The electrode orifices, distance to emitters, and size are all customizable thanks to the modularity of the design, which is compatible with any electrospray thruster type. The design provides alignment precision within 5 micrometers of the emitter tip and electrode orifice. While our new electrode achieved reproducible extraction, instability is still present. The data on emission from these emitter-electrode stacks is presented, as well as in situ microscopic optical observation of individual emitters. The images demonstrate emission in multiple extraction modes, microfluidic behaviour of the capillaries in space-like conditions, and interactions of the emission modes with the integrated electrode.

Keywords: Micropropulsion, Electrospray, 3D Microlithography, Additive manufacturing

Introduction

Electrospray thrusters belong to the electrostatic thruster family [1]. They are a promising option for micro propulsion applications, such as on CubeSats. Their scalability is a key factor driving the interest in these thrusters for micro and nano satellites [2–4]. Electrospray thrusters can be easily downscaled and even benefit from it, which sets them apart from more traditional electric propulsion systems like Hall thrusters [5]. Another reason is that depending on the system configuration a neutraliser can be omitted from the propulsion system, thus reducing the already low power requirements further [2]. Additionally they provide precise thrust and impulse bits, making them ideal for high precision manoeuvres like constellation flight. Another advantage is their use of liquid or semi-solid propellants. This property renders them highly manageable during launch and integration and the accessibility of the propellants is appealing for commercial applications such as mega constellations [5].

Electrospray thrusters operate by extracting ions or droplets from a liquid propellant using a static electric field. The fluid is deformed due to the electrical field and grows into a conical shape called Taylor-cone as the field strength is increased [2, 6]. At the Taylor-cone tip, the electric field density is sufficiently high to forcibly extract ions or droplets of the propellant from the fluid, causing them to accelerate alongside the electric field [7]. To function properly, the fluid must either be conductive or have a polar component such as water [6]. For most types of elctrospray thrusters, either liquid metal or ionic liquids are typically utilized as propellant. Liquid metal must first be heated to its melting point before use. Indium is commonly used due to its relatively low melting point of $150°C$ [8]. Ionic liquids, on the other hand, are salts that remain in a liquid state below room temperature [9–11]. Additionally, these liquids have very low vapour pressure, allowing them to remain stable in vacuum conditions [11]. Their composition of pure ions results in high electrical conductivity, making them an ideal propellant for electrospray thrusters. Moreover, the use of ionic liquids permits extraction of both positive and negative ion species, eliminating the need for an external neutraliser [12].

An electrospray thruster typically comprises three main components: the propellant intake, emitter structure, and extraction electrode. The propellant intake, which can be either a tubing system in actively fed thrusters or a reservoir in passively fed systems, provides the necessary propellant for the emitter structure. Once the fluid reaches the emitter structure, it is exposed to an electrical field, which facilitates ion extraction. There are three variations in the structure of the emitter, distinguished by the method of supplying propellant to the emission sites. The general operating principle remains the same for all three variations [13]. One type of emitter is the porous emitter, which delivers propellant through a porous base material from which the emitter structure is formed. Usually, a conical structure is used, although wedges or edges may also be effective for facilitating ion emission [12]. Another type of emitter is the external emitter, where the propellant is supplied to the base of an emission structure and is drawn up to the emission point by surface forces [13]. Similar to porous emitters, the conical shape is usually preferred. Another approach is the capillary emitter, also known as the internally wetted emitter [13, 14]. This type employs a capillary system to convey the propellant to the emission site. Each approach presents distinctive challenges. For instance, the arbitrary pore size and distribution of porous emitter structures render their reliable production almost impracticable. External emitters may have reduced emission predictability due to the extraction of secondary ions from the fluid between emitter structures. Capillary emitters are susceptible to overflow as a result of the capillaries' low hydraulic resistance [18]. The extraction electrode is the final component required for ion extraction. It functions as the liquid's ground reference and is essential for creating the electric field necessary for extraction. Typically, a metal lattice is used as the extraction electrode, which is positioned above the emitter structure [2].

In our work we focus on the additive manufacturing of miniaturised capillary type electrospray thrusters. We utilize a micro 3D printing technique, two photon lithography, to fabricate high aspect ratio capillary emitters structures as well as a newly developed fully modular extraction electrode.

Methods

In this paper, we present a fully modular design of an electrospray thruster and report on the results obtained from testing these emitters. The included data comprise scanning electron microscope images, optical images, and extraction data. In this section we want to focus on the fabrication and characterisation methods used to obtain the result presented later on.

Additive manufacturing

3D micro printing and capillary designs

Our new design builds upon our previous work [14, 16, 17], which employs the technique of two-photon laser lithography, an additive manufacturing process. As the name suggests, this method utilizes two-photon interactions to initiate chemical reactions in a photosensitive resin [14, 15]. A single photon carries too little energy to trigger a photochemical reaction, thus passes right through the photo resist without being absorbed. A reaction can occur only if two photons are simultaneously absorbed, which necessitates a sufficiently high intensity. Such intensities are attained by focusing the laser through microscope optics [14, 15]. At the lens' focal point, the beam is compacted into a minute volume, producing very high photon densities. Inside this small volume, referred to as a 3D pixel or voxel, two photon absorption can occur [14, 15]. By using negative tone photoresist, a hardened piece of epoxy is produced inside the voxel through photochemical reactions. A 3D structure can be created by scanning the voxel through the resist, either by moving the substrate with the resin or by changing the laser path via mirrors. This process closely resembles standard 3D printing. Depending on the photoresist and microscope lens used, lateral resolutions as low as 100 nm can be attained. In comparison to other micro mechanical fabrication techniques such as micro machining or etching, two-photon lithography presents significantly fewer constraints in terms of shape and structure possibilities [15]. Under-cut, asymmetric, and even hollow structures can be manufactured using this microfabrication technique, which is often difficult or outright impossible with other microfabrication techniques. Another advantage is the ability to fabricate structures with a high aspect ratio (width to height ratio). In our previous work, we demonstrated that it is possible to fabricate structures with capillary diameters of less than 10 μm and an aspect ratio larger than 20. This possibility is directly related to the capillary design employed for the emitters [14, 16, 17]. One of the major challenges with capillary type emitters is their hydraulic resistance [18]. If the emitters possess insufficient resistance, they are prone to overflowing or producing large droplets instead of a fine ion spray. To enhance the hydraulic resistance, one solution is to increase the aspect ratio of the capillary. The flow rate through a finite capillary is described by the Hagen-Poiseuille law.

$$\dot{V} = \frac{\pi \cdot r^4}{8 \cdot \eta \cdot l}(\Delta p). \tag{1}$$

The volume flow rate $\dot{V}$ is dependent on the capillary radius r, the viscosity of the fluid η, the length of the capillary l, and the pressure gradient between the input side

and output side $\Delta p = p_{in} - p_{out}$. For our purposes, we can generalize that the pressure on the output side p_{out} is nearly equal to zero since it is open to space.

This results in two categories of variables: those dependent on the emitter design, namely the radius and capillary length, and the system variables, such as fluid viscosity and input pressure. The radius exerts the greatest influence on flow rate, as it is proportional to the 4th power. Increasing the length of the capillary would also result in an increase in resistance. However, compared to the impact of the radius, the linear increase in length has a much smaller effect. The dependence on both the radius and the capillary length is the reason why a high aspect ratio is needed to achieve low flow rates, as both a smaller radius and a longer capillary decrease the flow rate.

IP-Q Material system

In our previous work, we utilized SU-8, a photoresist, as the base material for our emitter structures. SU-8 is renowned for its mechanical stability, high resistance to solvents and chemicals, and stability under space-like conditions [16]. We employed the NanoScribe™ PPGT, a 3D lithography device, to fabricate emitters and emitter arrays with aspect ratios ranging from 5 to 20. One of the significant drawbacks of working with SU-8 is resist preparation. SU-8 needs to be applied onto a silicon wafer by means of a spin coater, resulting in very smooth but rather thin resist films. The maximum attainable layer thickness with SU-8 is about $400\,\mu m$, which imposes a limitation on the maximum height of the emitter or any other structures. Consequently, we opted to use IP-Q resist, which was specially developed by NanoScribe™ for 3D lithography with their 'large feature solution' set. With IP-Q, structures up to 10 mm in height can be fabricated. IP-Q provides comparable mechanical and chemical properties to SU-8 and performs similarly as a base material for microfluidic applications. However, there are some variations in wetting angle and surface properties which require further investigation to arrive at a comprehensive comparison.

In addition, it is necessary to verify the radiation hardness of IP-Q for future applications. For now, IP-Q serves as a suitable replacement for SU-8. Another benefit of utilizing IP-Q is the significantly faster process time as a result of using a 10× objective instead of the previously used 20× objective. The process time has been reduced from 12 hours per emitter array to 4 hours per array. It should be noted that the higher printing speed is achieved at the expense of increased voxel dimensions. With the 10× objective, the lateral voxel size is about 1.5 μm, and the longitudinal size is about 25 μm. Although the lateral size is comparable to that of the 20× objective, the longitudinal size is approximately five times larger. This enlargement of the voxel size reduces the print resolution, resulting in a slight loss of print quality. However, this effect is negligible once accounted for. Figure 1 illustrates a capillary emitter example made with the 10× objective in IP-Q. The capillary has a diameter of 40 μm and a length of 300 μm. However, a change in material system from SU-8 to IP-Q necessitated a new examination of printing parameters and structure designs to obtain equivalent results to those previously achieved using SU-8. All in all, we can now manufacture emitters that have greater height and capillary length compared to the SU-8 process.
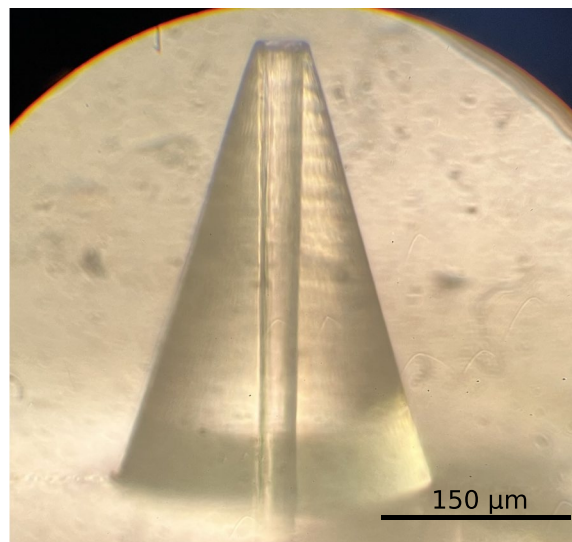
Fig. 1 Image taken through a optical microscope with a 50x magnification. The emitter is fabricated using 3D lithography in the large feature configuration and IP-Q resin. This design features a 30 μm diameter capillary with a length of 300 μm. Due to the parallax the capillary seems wider at the top, however SEM imaging shows a uniform capillary diameter over the whole length. We also included an image of an emitter with a 10 μm diameter capillary in Fig. 9 in the Appendix

Fully modular integrated extraction electrode

The decrease in printing time is a favourable outcome, but the primary incentive for transitioning to IP-Q was the increased structure height that could be achieved. Considering IP-Q, we developed and constructed an integrated extraction electrode for the emitter arrays. The integration of the electrode into the emitter design presents numerous advantages, such as enhancing the alignment accuracy between the emitter orifice and electrode, thus lessening the intercepted ion current. 3D printing the electrode further reduces fabrication errors. Such errors can result in differences in the extraction behaviour of emitters, due to the interaction of the emitters with the electrode. The compact design itself is another benefit, as the integrated electrode requires far less support material. The 3D lithography method ensures a manufacturing of multiple extraction electrodes that are nearly identical in size and shape and offers high flexibility to adapt the design of the electrode in any desired way.

One option for integration involves incorporating the electrode into the emitter array's design and printing them together in a single fabrication step. This approach yields optimal alignment and structural integrity at the cost of flexibility. Another consideration here is the metallization of the electrode. As the base material is the insulating IP-Q polymer, a secondary metallization process is necessary to produce a functional electrode. Directly printing the electrode onto the array can complicate this process. An alternative approach is to create a modular electrode that can be added to the emitter in a subsequent step. We chose this option because it is easier to incorporate into our current design and offers more flexibility.

In Fig. 2, a scanning electron microscope (SEM) image depicts the electrode mounted on an emitter. The image shows the design we developed for the electrode, which comprises three parts: the bottom layer, placed atop the emitter; several pillars, creating the
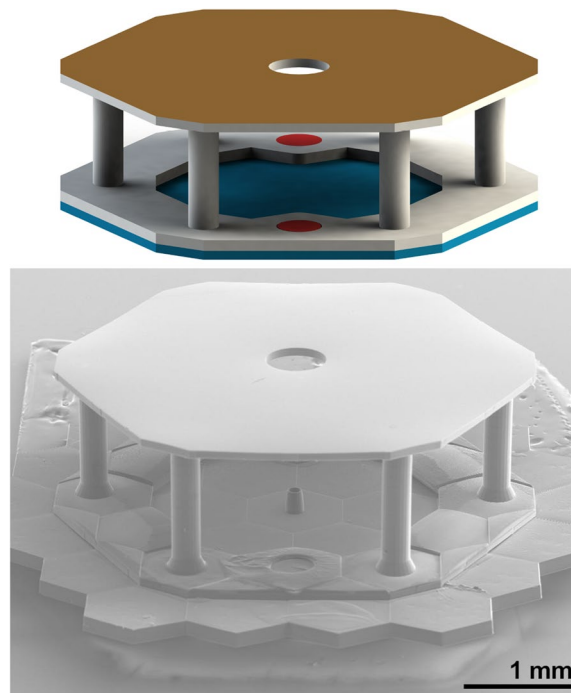
Fig. 2 A 3D rendering of the electrode structure and a scanning electron microscope (SEM) image depicting an emitter with the newly developed integrated extraction electrode. The 3D rendering is based on the same schematic used to fabricate the presented electrode, but does not include any emitter structure. In the rendering, the emitter base (blue), the alignment cones (red), and the electrode structure (white) are highlighted. The modular electrode is composed of the bottom layer, the spacer layer and the top layer which holds the metal film (yellow) that acts as the extraction electrode for the emitters. The SEM image gives an isometric view of the emitter-electrode pair based of the schematic presented above, revealing the electrode's placement on the emitter surface. In the forefront is one of two alignment cones visible that are affixed within the base of the electrode. The minor distortion adjacent to the cone is a result of the adhesive resin employed to fasten the electrode to the emitter

space between the emitter and the top layer; and the top layer, which carries the metal part of the electrode. Each layer is described in more detail below, starting with the top layer.

The top layer is 75 µm thick and contains emission apertures, with each aperture having a 500 µm diameter and centred on an emitter position. The number of apertures can be customized as per user requirements. Figure 3 depicts a single aperture, while Fig. 4 exhibits a design with seven apertures. The layer itself is composed of IP-Q polymer and is non-conductive; therefore, the top of the electrode needs to be metallized. Metallisation is carried out after the printing of the whole electrode structure and is done using a thermal evaporation apparatus. Such a device is advantageous for metallizing as it solely coats one side with metal, keeping the other sides essentially metal-free which evades short circuits.

This method is commonly used in semiconductor manufacturing to apply metal coatings to microelectronic wafers. A piece of the chosen metal is placed in a tungsten carrier and heated under vacuum conditions until it evaporates, releasing metal vapour into the surrounding. The metal vapour's origin is positioned at such a distance from the structure that the particle flux can be assumed parallel when it reaches the sample, where it solidifies on the sample surface. The deposition produces
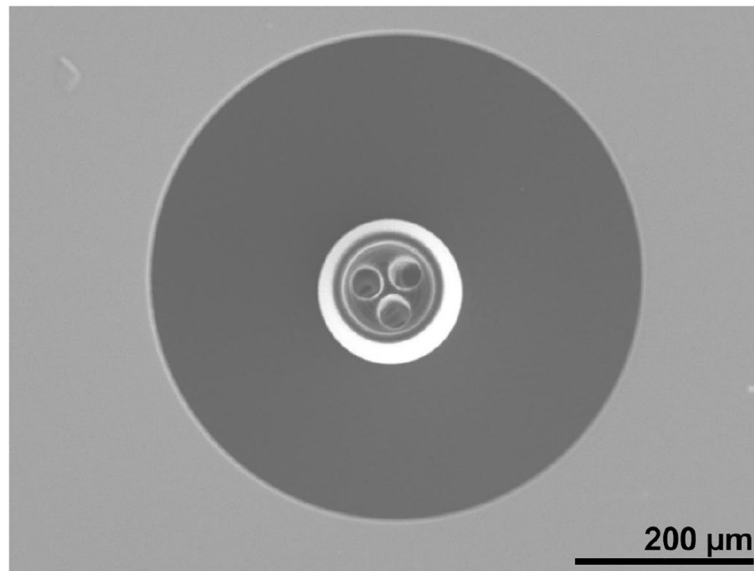
Fig. 3 Scanning electron microscope image giving a top-down view of the emitter and the electrode aperture with a highly aligned appearance. The emitter, in this case a three-capillary design, is centred on the aperture with very little divergence from the center position
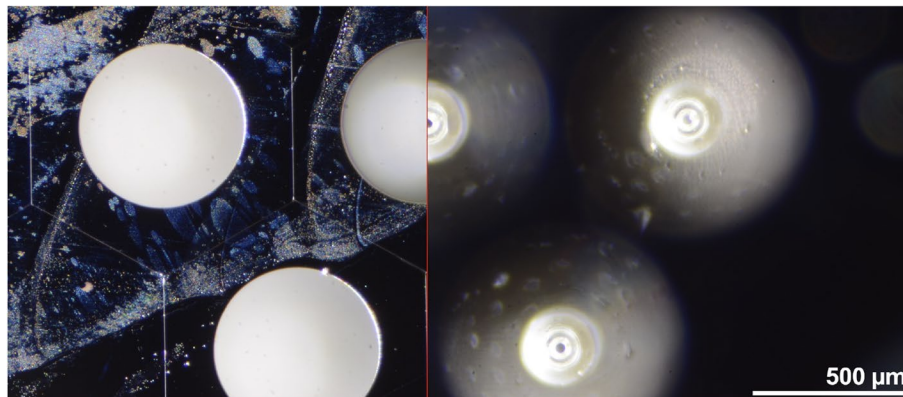

Fig. 4 The two optical microscope images depict the same emitter array with an integrated electrode. The images were taken without moving the sample and only adjusting the focal plane. For clarity, the two images are superimposed on top of each other, displaying only a portion of each image. In the left section of the image, the surface of a metallized electrode is in the focal plane, and the aperture through which ions exit the thruster is prominently visible. In the right portion of the image, the emitter tips are situated in the focal plane. Small black dots in the center of the emitter tip indicate the visible capillary openings. The near-perfect alignment between the emitter and the electrode is observable due to the stacking of the two images. The capillary orifice is precisely centered on the electrode aperture

a shadow-casting effect similar to a light source, resulting in only the surface facing the vapour's origin being coated. This is one reason why a modular system was chosen, because with a modular design it is possible to coat the electrode structure separately, thus avoiding an unintentional coating of the emitters through the extractor holes. Such a metal coating on the emitters may affect their wetting behaviour and increase the chance of propellant overflow to the surface or short circuits due to the conductive metal layer. Another factor to consider is the slight variation in the

Kunze *et al. Journal of Electric Propulsion* (2024) 3:3

Page 8 of 19

thickness of the metal coating. While these variations are negligible in case of the extraction electrode since they are very small compared to the distance to the emitter, they may result in significant variations in wetting behaviour and interaction with the liquid propellant near the emitter making the emitters less comparable even within the same production batch. Masking the emitters under the extractor to avoid uncontrolled coating would be a significant challenge, but the modular design circumvents this challenge. For enhancing the metal's adherence to the polymer, we initially incorporate a thin layer of chromium measuring 2-5 nm, succeeded by a silver layer measuring 150-250 nm. The metal layer is sufficiently thick to cover the entire surface, and the high conductivity of silver guarantees a uniform electrical field.

The spacer layer is the second layer that provides mechanical stability and secures the metallized layer in place. It comprises several round pillars with a 300 µm diameter, ensuring the necessary stability while enabling nearly unobstructed observation of the emitter. Although the stability could be enhanced by using full walls, we opted for a visually open design. The visual open design was chosen for the in-situ observations. Full walls would indeed increase the mechanical stability, however, would also block any view to the emitter structures. For a finalised design a full wall adaptation would surely be beneficial. The added mechanical resilience would be useful for the strong forces and vibrations on launcher start. The height of the pillar can be adjusted to determine the distance between the emitter tip and metal electrode. This flexibility in height allows for customization of the electrical field distribution between the emitters and electrode, and the maximum extraction voltage, to meet the specific needs of the application.

The bottom layer serves as the connection point between the emitter and the electrode, determining their alignment. For optimal alignment, we have incorporated a self-aligning feature consisting of two conical markers printed on the emitter array surface. These markers are added after the printing of the emitter structure and possess no impact on the emitters themselves. There are two openings in the bottom layer of the electrode that securely fit onto the surface markings of the emitter, which makes the integration process straightforward, resembling the use of building blocks. The conical shape of the markers and the extremely precise tolerances result in a perfect alignment of the electrode with the emitters, as shown in Figs. 3 and 4. These images illustrate the exceptional level of alignment attainable at an individual scale, however, the moment, we do not have enough data for providing meaningful statistical data concerning the coaxiality deviation after assembling extraction electrode and emitter structure. For a more detailed image of the alignment we refer to Fig. 10 in the Appendix.

The design of the extraction electrode is completely modular and can be applied to any of our manufactured emitter arrays. It provides a wide range of options, thanks to its adjustable number of apertures, aperture diameters, and height, for matching the electrode design to the emitter array or specific applications. Alignment of the openings to the emitters is ensured by the conical indicators and can be accurately replicated. In addition, the ability to observe the emitters during operation is facilitated by the high visibility in the space between the emitter and electrode. Furthermore, the electrode design is not directly linked to the emitter design, indicating its suitability also for externally wetted or porous type emitters. With its modular design it can be easily adapted to other types of electrospray thrusters.

Kunze *et al. Journal of Electric Propulsion*   (2024) 3:3

Page 9 of 19

In situ microscopical optical observation

Miniaturization is advantageous for electrospray thrusters, as previously stated [5]. Nevertheless, this creates challenges in characterizing the fabricated emitters. Due to their small size and the vacuum environment in which they are tested, standard optical observation is not always feasible for gaining insight into functionality and extraction behaviour on a microscopic scale. There are numerous variables that may influence emitter emission behaviour, such as extraction voltage, feed rate for actively fed systems, emitter geometry, and electrode spacing, among others. Determining the influence of emitter design is particularly difficult by electrical characterization alone.

For better understanding of the interplay between variables, we will be employing two optical cameras. One camera, a basic optical USB camera with adjustable focus, is employed to capture real-time footage of the entire emitter stack. Its purpose is to record the fluid intake and the interaction between extracted ions and the electrode as a whole. The second camera is a high-resolution black and white camera with an interchangeable adapter for a microscope objective. We can fit objectives that magnify 5× to 50× on the camera to focus on specific parts of the emitter. Using 10× magnification, we can observe multiple emitters of the array while still being able to resolve the emitter tip with the extraction site. With this dual camera set-up, we can observe the emitter stack at both macro and micro levels in real-time. This facilitates correlation of optical data obtained from the cameras with the emission data obtained from electrical characterization. One significant benefit of utilizing a camera set-up with capillary-type emitters is the ability to observe the microfluidic behaviour of capillaries. As fluidic resistance presents a major challenge for capillary-type emitters, observing capillarity in situ helps significantly in designing the emitters to meet desired parameters. Moreover, these capabilities are not limited to capillary-type emitters exclusively. For example real-time optical observation can assist in pinpointing the root causes of secondary emission site formation between emitters or the interaction between the fluid and the electrode in external wetted designs. This type of observational method has numerous applications, beside the already discussed ones.

Active fluid feeding under vacuum conditions

To achieve a representative simulation of space-like conditions, we utilize a vacuum chamber to test the emitter arrays. However, the fluid supply under such conditions present a significant challenge. Various methods exist for vacuum liquid propellant feeding. One such method involves utilizing capillary forces in porous materials to passively pull liquid from a reservoir to the extraction sites [13, 19]. Passively-fed systems are low in complexity and contain no moving parts. The material's self-regulation is due to capillary forces that contain the propellant. However, it does not provide control over fluid intake and distribution. It was reported, that the thruster performance correlates with the reservoir fill levels, resulting in loss of performance over time with less liquid remaining inside the tank [19]. Additionally, manufacturing the emitters to achieve equal liquid distribution along the emitter array is complex and costly. Unequal distribution would also negatively impact the performance [19].

One way to actively control fluid feeding is by using a gas-powered system. The system includes a reservoir with one open side that is placed in a pressure container, which

can be evacuated or flooded with a gas. A capillary is connected to another side of the reservoir, leading to the electrospray thruster [20–22]. The pressure inside the container can be controlled to regulate the fluid's flow rate into the capillary. Though effective, this method is complex. The regulation of pressure must be exact requiring high pumping power for rapid pressure relief. Additionally, precise control of the gas used to increase the pressure is required [20]. A further concern is the potential for gas to dissolve into the liquid and degas inside the thruster later on.

A second means of precisely managing flow rate is utilizing a precision pump. We already have successfully utilized this methods in the past, achieving favourable outcomes [14, 16, 17]. Utilizing a high-precision syringe pump enables us to effectively regulate the input rate via pump throttling. We can calibrate the flow rate, which corresponds to the pump throttle, using a mass flow meter. This guarantees that the appropriate amount of fluid is delivered to the emitter, providing full control over the feeding process. However, there remains a pressure difference issue when the pump holding the syringe is at ambient pressure. A minor leak of fluid from the outside into the emitter due to this pressure difference was detectable by the mass flow meter. To address this issue, a shut-off valve was utilized. Another issue that arose over time was the accumulation of air in the system, despite the use of gas-tight fittings and syringes. This led to spontaneous degassing within our emitter arrays, which disrupted testing. Therefore, we adapted our pump to function under vacuum conditions and relocated the entire feeding system to the inside of the vacuum chamber. A schematic diagram of the modified arrangement is presented in Fig. 5. A second modification was made to the syringe in order to allow gas to escape during vacuum chamber evacuation.

This involved shortening the syringe to enable complete plunger extraction during pump down, which exposes the fluid inside the syringe to the chamber. Once a pressure of less than $1 \cdot 10^{-4}$ Pa was reached, the plunger could be pushed back into the syringe, effectively sealing it. A special guiding attachment ensures correct plunger insertion. This arrangement allows for precise feeding rate control during operation, while also guaranteeing that no gas is fed to the emitter.

Results

Optical images and videos of emitter operation and in-situ observation as well as emission data are presented. In all experiments, the electrode is grounded and then either a positive or negative high voltage is applied to the ionic liquid, 1-ethyl-3-methylimidazolium tetrafluoroborate (EMIM-BF$_4$). All data including the video files and the corresponding extraction data, is available according to the FAIR regulations in our data repository [23]. The data presented here is for three emitter designs with different geometries. The individual characteristics of each design can be found in Table 1 and are further discussed in more detail in the corresponding section. For each design, a 3D render showing a cross-section of the capillary structure is available in our data repository [23].

The emitter designs and the corresponding data presented here were chosen from multiple experiments conducted on samples with similar or identical geometries. All results are reproducible for emitters of identical capillary configuration and of each design.

Figure 6 displays multiple images captured from a video segment spanning approximately one second in time as well as the correlating emission data. The three optical
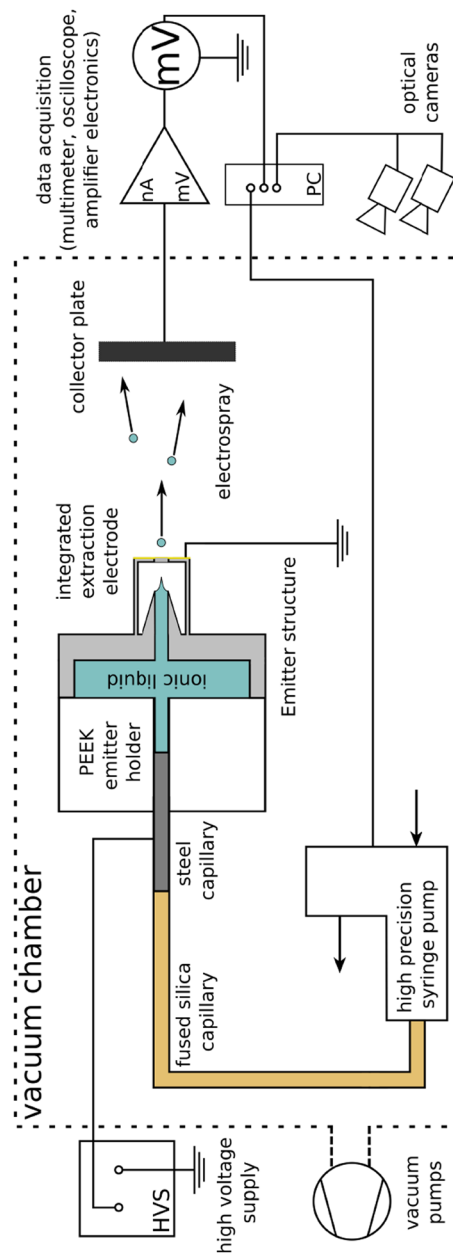
Kunze *et al. Journal of Electric Propulsion* (2024) 3:3

Page 11 of 19

Fig. 5 Schematic diagram of the measurement setup used. The setup resembles the one reported earlier [17], but with a few adjustments. The lower right portion of the diagram illustrates the recently integrated optical observation with two cameras. Furthermore, the fluid feeding system, including the tubing and pump, has been placed inside the vacuum chamber, hence is exposed to the vacuum

Table 1 Design parameters for the presented emitter structures

	Capillary type	Capillary length	Capillary diameter	Special notes
Design 1	straight circular	100 μm	20 μm	conical opening at
		200 μm	max. 40 μm	the emitter tip
Design 2	straight circular	300 μm	30 μm	
Design 3	straight rectangular	300 μm	15 μm×30 μm	five capillaries
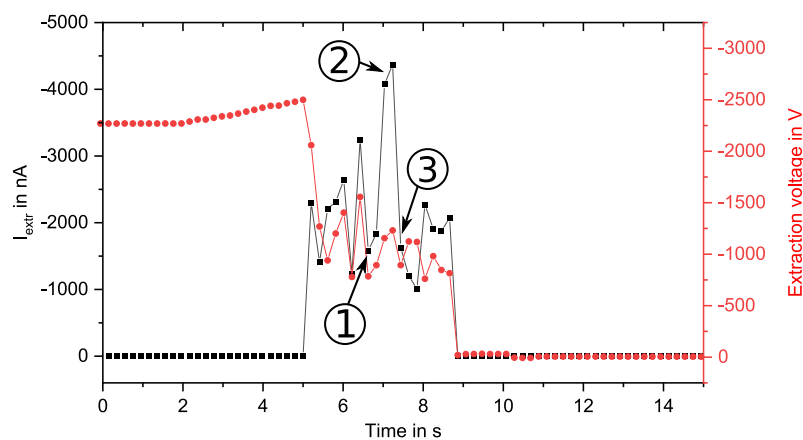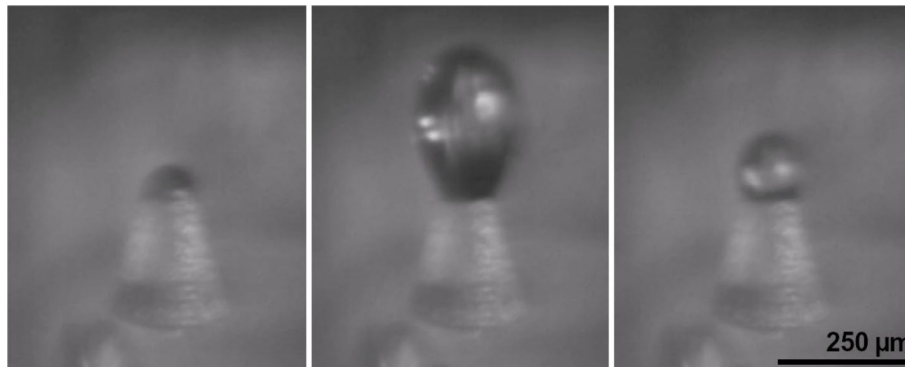
Fig. 6 Three optical images captured from a live video of an emitter array as well as the correlating emission data is shown. The pictures are arranged in chronological order, with the first one being on the left and the latest on the right. The time elapsed between the left and right image is estimated to be about one second. For this emitter, we opted for a design featuring a straight capillary that opens conically at the tip. The diameter measures 20 μm at the narrowest point and 40 μm at the tip. The image on the left depicts the droplet formation on the emitter tip while the capillary in the center of the emitter supplies the required fluid. In the middle image, the droplet is drawn towards the integrated extraction electrode while remaining connected to the emitter, taking on a raindrop-like shape. The right image depicts the same droplet, which has now significantly reduced in size and returned to the emitter tip, forming a spherical shape. Below the optical images the correlating emission data is plotted. On the horizontal axis is shown the time, which was normalized to improve the readability of the time frame of the extraction event. The time origin was arbitrarily chosen to fit the image data and set to 0 for visualisation reasons. The applied high voltage (red dots) and the converted extraction current (black squares) are plotted on the Y-axis. The emission correlating the images is represented by the numbers plotted into the graph, with 1 corresponding the left most picture and 3 to the right one

images are arranged in chronological order from left to right. The images show a single emitter of an emitter array, which features a straight, round capillary with a diameter of 20 μm and which opens conically at the tip to a diameter of 40 μm. The conical opening at the tip allows fluid to build up in this area.

The capillary's length totals 300 μm with 100 μm having a diameter of 20 μm. The correlating electrical emission data taken at the same time frame is plotted below the images. In the graph the extraction voltage and collected currents are plotted versus time. For visibly reasons the staring time was arbitrarily set to 0. The data shown confirms an extraction event happening in the time frame depicted by the optical images. During the experiment, a voltage was applied once a droplet was observed at the emitter tip. The point in time when the voltage was first applied lies outside the presented time frame. Slow, incremental increases in voltage were made until extraction was detected. This process took place over several minutes to allow the system to adjust accordingly. At the 2-second mark, a new voltage target was set, and the extraction voltage was slowly increased to reach the new target. For this experiment a negative voltage was applied to the ionic liquid. The extractor electrode and collector plate were at ground potential.

From the left to the right, one can see the formation of a small droplet in the cone shaped tip of the emitter. It is not visibly deformed and sits close to the tip. In the middle image, the droplet is significantly enlarged and seems to be drawn towards the extraction electrode. Compared to the previous image, the droplet has greatly increased in volume, and a significant portion of the fluid is suspended in the vacuum above the tip, while only a small part remains attached to the emitter. The droplet then returns to a smaller size, comparable to the droplet seen in the first image. This change can be observed in the right picture. However, there is still an apparent attraction exerted on the droplet, as it maintains a spherical shape rather than collapsing into a meniscus. The numbers plotted in the bottom section of Fig. 6 correlate with the chronological order of optical images with 1 denoting the left picture and 3 the right. The three images only capture a brief interval of the complete extraction process while the extraction data gives a complete overview of the extraction event spanning over seven seconds. The extraction
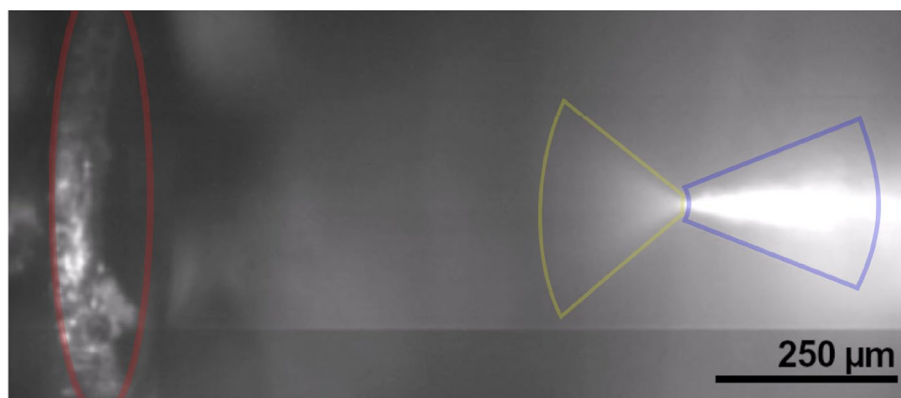

Fig. 7 One optical image obtained from live footage of an emitter array and the correlation extraction data. The integrated extraction electrode (marked in red) is visible on the left side and an emitter (marked in blue) in the right portion, which features a straight capillary with a diameter of 30 μm and a length of 300 μm. The image portrays the extraction of EMIM-BF$_4$ from the tip of the same emitter in the form of a fine spray (marked in yellow)

event was ultimately terminated when the ionic liquid overflowed onto the emitter surface, which was accompanied by multiple arc hits on the emitters.

The second dataset consists of a single optical image extracted from live footage. This picture shows a fine mist being extracted from an emitter, displayed in Fig. 7. The emitter on the right produces an ion spray aimed at the extraction electrode situated on the left side of the image. For this experiment we utilized an emitter featuring a straight capillary with a fixed diameter of 30 µm and a length of 300 µm. The emission data that was collected is not available due to a device error in the amplifier electronics. The high currents from the extraction event caused a safety shut-down of the amplifier. The emission was terminated by violent arcing which caused damage to the emitter. We believe that the reason for the termination in this case was a combination of the significant currents, the clearly visible spray in Fig. 7, and too high extraction voltages. This combination most likely caused the arcing we observed.

The last dataset consists of one optical image and the correlation emission data of the extraction event. The optical image in Fig. 8 displays an emitter and extraction electrode on the right and left, respectively. The emitter design incorporates five rectangular capillaries arranged in a star shape pattern. Each capillary has dimensions of 15 µm x 30 µm x 300 µm for length, width, and height, respectively. The image shows a fully formed Taylor-cone.
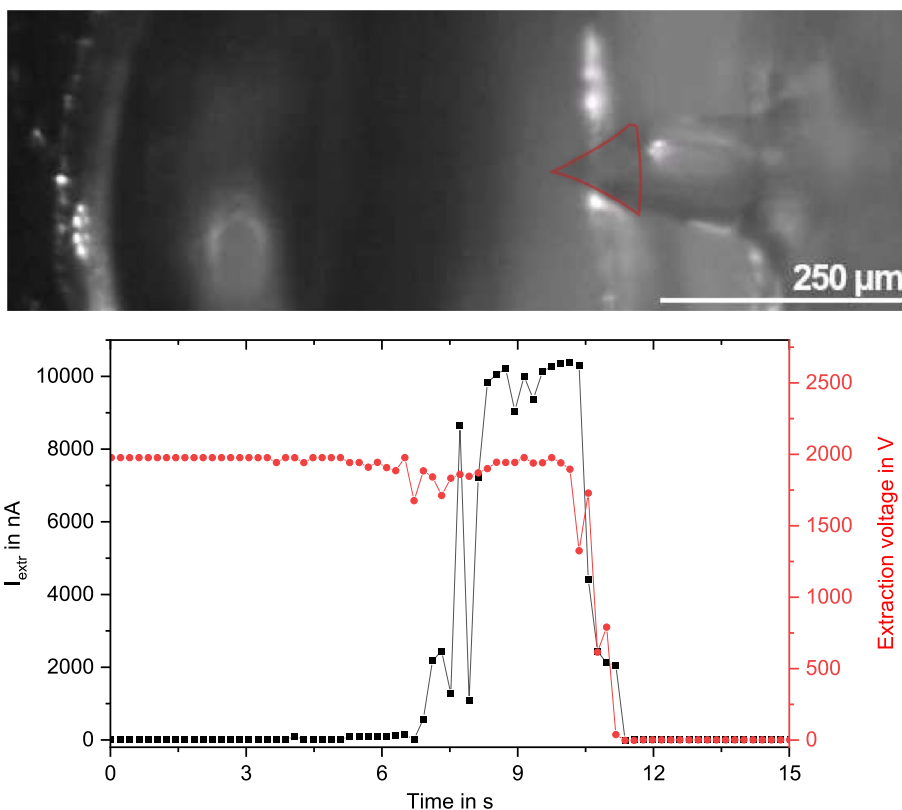

Fig. 8 An optical image captured from a live video of an emitter array, which shows an emitter and an extraction electrode aperture. The emitter consists of five rectangular capillaries arranged in a star pattern, each measuring 15 µm x 30 µm . The image displays a fully formed Taylor-cone positioned over the one of the emitters and oriented towards the extraction electrode. For better visualisation the outline of the Taylor-cone was retraced by a red line. Additionally, the Taylor-cone is observed to be centred to the electrode aperture. In the bottom half the extraction data is presented, with the normalized time plotted on the X-axis and the applied high voltage and the converted extraction current plotted on the Y-axis

For visibility purposes the outline of the Taylor-cone was enhanced with an red line in Fig. 8. The Taylor-cone in the image is positioned on the emitter such that it points directly at the extraction electrode. A slight reflection at the edge of the emitter tip reveals the bottom part of the Taylor-cone. Figure 8 also shows the correlated electrical emission data. Similar to the other experiments the extraction voltage was applied once the presence of fluid in the reservoir behind the emitter was confirmed in the camera image. The voltage was then slowly raised over the span of several minutes and after each incremental increase the system was given time to adjust to the new voltage. During this experiment a positive voltage was applied to the ionic liquid. The extractor electrode and collector plate were both at ground potential. The extraction event plotted in Fig. 8 took place in the adjustment process. The image shown in Fig. 8 can be placed around the nine second mark. The data exhibits very high emission with a maximum of 10 µA, which remains relatively stable from eight seconds to ten seconds. The extraction voltage is also stable at approximately 1.7 kV during this period. After ten seconds of emission, instability occurred which resulted in an arcing. This is reflected by the fluctuations observed in the high voltage and the exaction current.

Discussion

From the data obtained we can identify different extraction behaviour for the three emitter designs. The images and data in Fig. 6 strongly imply a droplet extraction mode featuring large droplets. This can also be seen in the emission data plotted in Fig. 6, which shows multiple peaks. It can be inferred from the images that significant portions of the droplet are detached during the process of being attracted towards the electrode. After losing a considerable amount of volume, the droplet descends back towards the emitter, possibly due to an imbalance of positive and negative ions within the fluid. This may also account for the reduced attraction observed following the droplet's split. Subsequently, new negative ions are attracted through the capillary, resulting in the formation of a new, large droplet. The video demonstrates the repetition of the cycle depicted in the three images. The extraction was stopped after a significant amount of fluid overspilled onto the surface of the emitter structure, wetting the complete space between the individual emitters. The observed behaviour suggests that the fluid resistance of the design presented, is still too low which is very likely also the cause of the overflow. The capillary is capable of drawing a significant amount of fluid in a short period of time, which favours droplet formation. Another inference can be made in regard to the design featuring a conical opening at its tip. Its intended purpose was the creation of a buffer zone for the fluid, thus reducing the chance of overspilling. However, it appears to have a detrimental effect on extraction behaviour since it promotes droplet formation at the tip. A notable observation can be made from the correlated video and emission data. The droplets appear to have significant mass but low charge. The level of extraction current in the emission data in Fig. 6 does not match the mass loss of the droplet. This phenomenon may be explained by the size of the droplet, which likely contains nearly equal amounts of negative and positive ions, with one type being slightly more dominant. As a result, there is enough attraction towards the electrode, but the measured currents are low. From the observations, one can gain significant insight into the interaction between the ionic liquid, emitter, and electrical field. The influence of the emitter design is also apparent from the images and the emission data. Unrelated to the emitter

design, the image sequence proves that the integrated electrode design is working as intended. The droplet is pulled towards the electrode aperture and shows very little tilt. This indicates a stable and well defined electrical field between emitter and electrode. Furthermore, the droplets are able to exit the emitter stack and reach the detector plate.

This influence is also evident in Fig. 7. The emitters implement a revised design that omits the conical buffer zone at the tip. A comparison of the emission behaviour depicted in Figs. 6 and 7 reveals the effect. The latest design shown in Fig. 7 does not exhibit droplet extraction, but instead shows a fine spray. This spray is indicative of a fine droplet emission or even purely ionic emission. Further validation of the emission data is necessary. As previously described, data collection was unsuccessful due to over-current in the amplifier electronics. However, the high currents, which are typical for pure ionic extraction, support this interpretation. This image also demonstrates the successful application of the recently developed electrode design. The spray pattern visible at the emitter tip exhibits symmetrical behaviour towards the aperture and points precisely at the opening. This observation further strengthens our hypothesis about the electric field distribution between the emitter and the electrode. Additionally, substantial currents were able to exit the electrode and reach the detector, even overpowering the electronics. The picture suggests a need for further investigation of the influence of the capillary on the emission. A white flash seen inside the emitter prompts uncertainty whether it reflects light from another emitter or if the spray is generated inside the capillary and, thus, glows. The implications for the design and the thruster as a whole are significant, depending on the circumstances.

As evidenced by the preceding images, Fig. 8 shows a clear Taylor-cone and confirms again the successful implementation of the electrode design. In this case, the ionic liquid is also pulled toward the electrode, even forming a complete Taylor-cone. The accompanying emission data corroborates this, as a substantial current was collected during cone formation.

As stated in "Results" section, the emission was terminated by instabilities which resulted in arcing. We hypothesise from the image data captured, that in this case too much fluid was pulled from the reservoir and caused an overflow. The extraction data also suggest that the Taylor cone collapsed rather spontaneously, thus terminating the extraction. Another explanation could be residual gas inside the reservoir which exited the array through one of the emitters. While rare, we observed that some gas may be captured inside the reservoir and may be extracted by the moving fluid. A spontaneous decompression of the gas could also lead to a collapse of the Taylor cone and cause arcing.

The data shown in Fig. 8 serves as an example of fluid-induced start-up, where voltage is applied before the fluid can reach the emitter tip. Investigations of fluid-induced versus voltage-induced start-ups reveal significant differences [24]. In certain situations, one method of starting a the thruster may be more advantageous than the other. Another important factor to consider is the design of the emitter. The rectangular capillary approach was used in this case, which is exclusive to this manufacturing method. This highlights the importance of innovative thinking when designing emitters. Exploring the various shapes and design features possible through 3D lithography could lead to unforeseen outcomes and benefits.

Conclusion

We introduced a completely modular design for extraction electrodes and its manufacturing process, which can be personalized to fulfil the requirements of the users while remaining compatible with any electrospray emitter. Moreover, we displayed the self-aligning ability of our design and demonstrated its implementation and integration into our electrospray emitter arrays through SEM and optical images. Additionally, we presented a new technique for acquiring in-situ video data of electrospray emitters and showcased the outcomes. We modified and created various emitter designs that utilized the IP-Q resin. These emitters were then subject to characterization by using optical videos and electrical emission data. Although emission behaviour remains unsteady, we are optimistic that stable emission will be achieved by refining our techniques in accordance with the IP-Q material system and adjusting the emitter designs. Once stable emission is confirmed, time-of-flight data will be collected to analyse the performance of the thruster. We also want to investigate the influence of different ionic liquids on the emission behaviour.
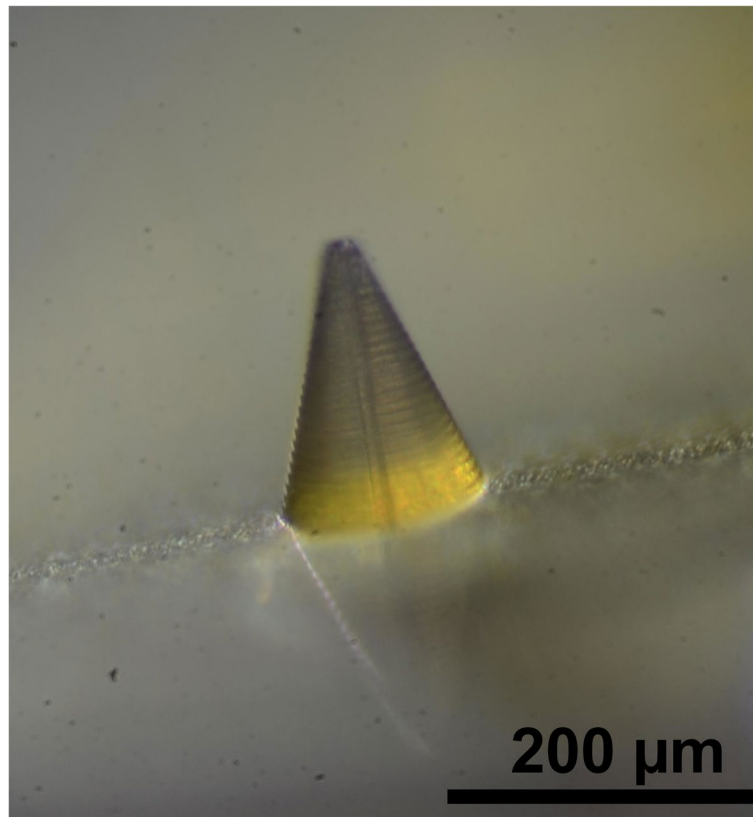
Appendix A Additional figures

Fig. 9 A microscope image of an IP-Q emitter. The emitter features a 10 µm capillray diameter over a hight of 300 µm. The lower part of the emitter is obscured by the emitter base and only a 200 µm secton of the capillary is visible
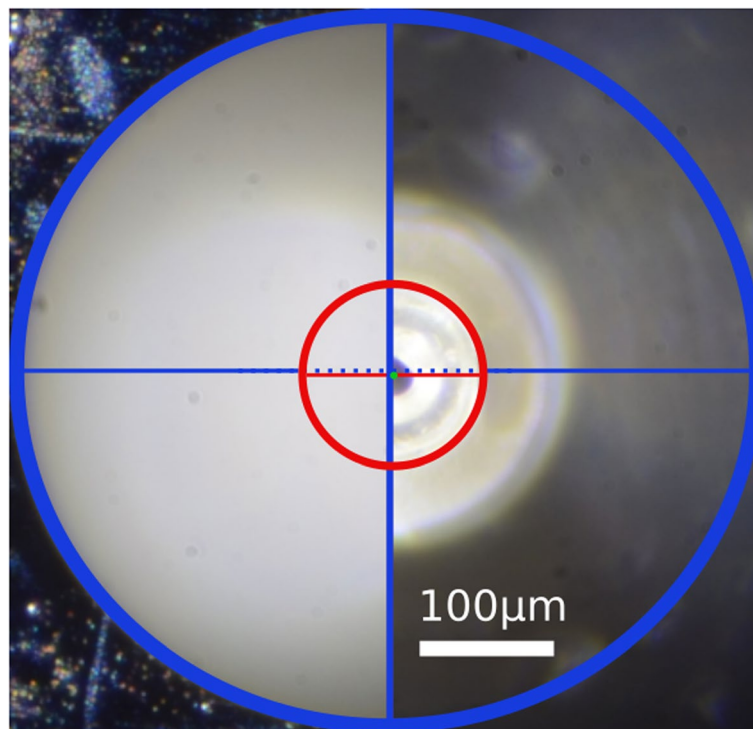
Fig. 10 Supplementary for Fig. 4. The picture shows a magnified section of the microscope image presented in Fig. 4 with additional markings. The blue cross-hair is aligned to the extractor orifice and the red cross-hair to the emitter structure. The small green dot in the center of the image marks the center of the capillary opening. From this picture the alignment quality of the emitter-extractor combination can be determined. The deviation of the center of the capillary from the center of the extractor orifice measures approximately 5 μm

Availability of data and materials
All data is publicly available under the FAIR regulations for data availability [23].

Code availability
Not applicable.

Declarations

Competing interests
The authors declare no competing interests.

Kunze *et al. Journal of Electric Propulsion*   (2024) 3:3

Page 19 of 19

References

1. Lozano PC, Martínez-Sánchez M, Hruby V (2010). Electrospray Propulsion. https://doi.org/10.1002/9780470686652.eae121

2. Lemmer K (2017) Propulsion for CubeSats. Acta Astronautica 134:231–243. https://doi.org/10.1016/j.actaastro.2017.01.048

3. Holste K, Dietz P, Scharmann S, Keil K, Henning T, Zschätzsch D, Reitemeyer M, Nauschütt B, Kiefer F, Kunze F, Zorn J, Heiliger C, Joshi N, Probst U, Thüringer R, Volkmar C, Packan D, Peterschmitt S, Brinkmann KT, Zaunick HG, Thoma MH, Kretschmer M, Leiter HJ, Schippers S, Hannemann K, Klar PJ (2020) Ion thrusters for electric propulsion: scientific issues developing a niche technology into a game changer. Rev Sci Instrum 91(6):061101. https://doi.org/10.1063/5.0010134

4. Lev D, Myers RM, Lemmer KM, Kolbeck J, Koizumi H, Polzin K (2019) The technological and commercial expansion of electric propulsion. Acta Astronautica 159:213–227. https://doi.org/10.1016/j.actaastro.2019.03.058

5. Gomez Jenkins M, Krejci D, Lozano P (2018) Cubesat constellation management using ionic liquid electrospray propulsion. Acta Astronautica 151:243–252. https://doi.org/10.1016/j.actaastro.2018.06.007

6. Taylor GI (1964) Disintegration of water drops in an electric field. Proc R Soc Lond Ser A Math Phys Sci 280(1382):383–397. https://doi.org/10.1098/rspa.1964.0151

7. Liu X, Deng H, Sun Y, Kang X (2022) Simulation of liquid meniscus formation in the ionic liquid electrospray process. Plasma Sci Technol 24(7):074008. https://doi.org/10.1088/2058-6272/ac61c0

8. Krejci D, Reissner A, Seifert B, Jelem D, Hörbe T, Plesescu F et al (2018) Demonstration of the ifm nano feep thruster in low earth orbit. In: 4S Symposium, Sorrento, Italy. https://www.researchgate.net/publication/325486881. Accessed 20 Sept 2023

9. Holbrey J, Seddon K (1999) Ionic liquids. Clean Prod Process 1:223–236. https://doi.org/10.1007/s100980050036

10. Rebelo LPN, Canongia Lopes JN, Esperança JMSS, Filipe E (2005) On the critical temperature, normal boiling point, and vapor pressure of ionic liquids. J Phys Chem B 109(13):6040–6043. https://doi.org/10.1021/jp050430h. PMID: 16851662

11. Chiu YH, Dressler R (2007) Ionic Liquids for Space Propulsion, vol 975. pp 138–160. https://doi.org/10.1021/bk-2007-0975.ch010

12. Guo Y, Sun W, Sun Z, Wu Z, He J, Yang C, Wang N (2023) Direct thrust test and asymmetric performance of porous ionic liquid electrospray thruster. Chin J Aeronaut 36(4):120–133. https://doi.org/10.1016/j.cja.2022.09.007

13. Peter BS, Dressler RA, Chiu Yh, Fedkiw T (2020) Electrospray propulsion engineering toolkit (ESPET). Aerospace 7(7). https://doi.org/10.3390/aerospace7070091

14. Kunze FL, Henning T, Klar PJ (2021) Taking internally wetted capillary electrospray emitters to the sub-ten-micrometer scale with 3D microlithography. AIP Adv 11(10):105315. https://doi.org/10.1063/5.0066619

15. Harinarayana V, Shin Y (2021) Two-photon lithography for three-dimensional fabrication in micro/nanoscale regime: a comprehensive review. Opt Laser Technol 142:107180. https://doi.org/10.1016/j.optlastec.2021.107180

16. Kunze FL, Henning T, Klar PJ (2022a) Validation of pure SU-8 micro 3D printed internally wetted capillary type electrospray mircoemitters for thruster applications. 8th internatinonal conference on space propulsion, Estoril (SP2022-082)

17. Kunze FL, Henning T, Klar PJ (2022b) 3D micro printed internally wetted capillary type electrospray emitters on the single micrometer scale. 37th International Electric Propulsion Conference (IEPC), Boston (IEPC-2022-175)

18. Gustan-Gutierrez E, Gamero-Castaño M (2017) Microfabricated electrospray thruster array with high hydraulic resistance channels. J Propuls Power 33(4):984–991. https://doi.org/10.2514/1.B36268

19. Chen C, Chen M, Zhou H (2020) Characterization of an ionic liquid electrospray thruster with a porous ceramic emitter. Plasma Sci Technol 22(9):094009. https://doi.org/10.1088/2058-6272/ab9528

20. Ma C, Messina V, Ryan C, Rovey JL, Putnam ZR, Lembeck MF et al (2022) Emission characterization of porous electrospray thrusters with actively controlled flow rate. https://eprints.soton.ac.uk/474346/. Accessed 14 Sept 2023

21. Demmons NR, Wood Z, Alvarez N (2019) Characterization of a high thrust, pressure-fed electrospray thruster for precision attitude control applications. AIAA 2019–3817. https://doi.org/10.2514/6.2019-3817

22. Zhang K, Kuang S, Suo X, Huang X, Li Z, Wang D, Jia H, Tu L, Song P (2022) Analysis of beam currents under an oscillating cone-jet mode for developing high-precision electrospray thrusters. J Appl Phys 131(9):094501. https://doi.org/10.1063/5.0083210. https://pubs.aip.org/aip/jap/article-pdf/doi/10.1063/5.0083210/16505945/094501_1_online.pdf

23. Kunze FL (2023) Data for '3D micro printed capillary electrospray thruster with a fully modular integrated extraction electrode'. JLUpub. https://doi.org/10.22029/jlupub-17893

24. Uchizono NM, Collins AL, Thuppul A, Wright PL, Eckhardt DQ, Ziemer J, Wirz RE (2020) Emission modes in electrospray thrusters operating with high conductivity ionic liquids. Aerospace 7(10). https://doi.org/10.3390/aerospace7100141

Publisher's Note